Wear, Vol. 267, Issue 12 (2009), p. 2186-2199
doi:10.1016/j.wear.2009.09.012

Development of a Fretting-Fatigue Mapping concept: Impact of material properties and Surface treatments

S. Fouvry*, K. Kubiak

LTDS, CNRS, Ecole Centrale de Lyon, Ecully 69134 Cedex, France

krzysztof@kubiak.co.uk

Abstract

Fretting fatigue induced by combined localized cyclic contact motion and external bulk fatigue loadings may result in premature and dramatic failure of the contacting components. Depending on fretting and fatigue loading conditions, crack nucleation and possibly crack propagation can be activated. This paper proposes a procedure for estimating these two damage thresholds. The crack nucleation boundary is formalized by applying the Crossland high cycle fatigue criterion, taking into account the stress gradient and the ensuing "size effect". The prediction of the crack propagation condition is formalized using a short crack arrest description. Applied to an AISI 1034 steel, this methodology allows the development of an original Material Response Fretting Fatigue Map (FFM). The impact of material properties and surface treatments is investigated.

Keywords: Crack nucleation, Crack arrest, AISI 1034 steel, Surfaces treatments, Fretting.

1. Introduction

Fretting is a small amplitude oscillatory movement, which may occur between contacting surfaces that are subjected to vibration or cyclic stress. Combined with cyclic bulk fatigue loading, the so-called fretting-fatigue loading can induce catastrophic cracking phenomena which critically reduce the endurance of assemblies. Considered to be a plague for modern industry, fretting-fatigue is encountered in all quasi-static contact loadings subjected to vibration and cyclic fatigue and thus concerns many industrial branches (helicopters, aircraft, trains, ships, trucks, ….) [1, 3].

As illustrated in Figure 1, fretting fatigue loading can be characterized by the superposition of a heterogeneous cyclic stress gradient related to the contact loading, and a homogeneous fatigue bulk loading.

Indeed, the contact stress decreases asymptotically below the interface. From this typical stress distribution, cracking damage will evolve in three different ways. Below a threshold fretting fatigue condition, no cracks are nucleated and the system runs under safe crack nucleation conditions. Above this threshold, two evolutions can be observed: for intermediate loading conditions, a crack will nucleate; however, due to the very sharp decrease of the contact stress below the interface, it will finally stop. This typical behavior defines the safe crack arrest domain [3]. Imposing higher contact and/or bulk fatigue loadings, the nucleated crack cannot stop and will propagate until final failure is reached. This defines the ultimate failure domain.

During the past decades, a significant effort has been made to formalize both the crack nucleation and the crack arrest conditions. The crack nucleation phenomenon is commonly addressed by transposing conventional multiaxial fatigue criteria [4, 5]. Specific analysis has been devoted to formalizing the contact stress gradient effects (i.e contact size effect). Different approaches like determining an averaged stress state over a representative process volume [6, 7] but also "notch stress" similitude approaches have been developed [8, 9]. The crack arrest description has been formalized by computing the evolution of the stress intensity factor below the interface, and by predicting the crack arrest condition using short crack arrest formalisms derived from the Kitagawa and El Haddad models [10-12].

The objective of this work is to combine these two approaches in order to describe the different types of fretting fatigue damage through the synthetic form of a Fretting Fatigue mapping concept (Fig. 2). The three damage behaviors are reported as a function of fretting loading (Y axis) and fatigue loading (X axis).

Then the plain fatigue parameter along the X axis will be determined from conventional fatigue tests whereas the plain fretting damage along the Y axis will be identified from plain fretting conditions. Finally, the combined fretting-fatigue test will permit to be identified, respectively the crack nucleation and crack arrest boundaries in the intermediate domains. To rationalize this analysis, the fatigue stress amplitude is normalized by the fatigue limit (σ_a/σ_d) whereas fretting loading, restricted to the partial slip condition, is quantified though the ratio $Q^*/\mu P$. Like for any fatigue problem, the mean stress level plays a critical role in the damage evolution. Both fretting and fatigue loadings have therefore been related to the corresponding stress ratii R_Q and R_s respectively. To avoid any perturbation induced by this latter aspect, this investigation is developed for pure alternated stress conditions (i.e. $R=R_Q=R_s=-1$). By introducing this new mapping concept, the present investigation develops a combined

experimental and modeling methodology to identify the damage boundaries and to provide an explicit description of the various types of fretting-fatigue damage. Finally, the impact of material fatigue properties, but also various surface treatments like shot peening or HVOF coatings, is discussed and schematically transposed into the Fretting Map description.

2. Experimental conditions

2.1. Materials

Fretting Fatigue phenomenon involves numerous complex mechanisms, which is why, to establish a predictive methodology, the investigation must be calibrated on a well known material. The material used for the experimental investigation and the construction of the model is a low carbon steel alloy, AISI 1034. Fully investigated by Gros [13], it displays a ferrite-perlite structure with the mechanical and fatigue properties listed in Table 1.

To investigate material property effects, the global fretting fatigue response of a low alloyed steel 30NiCrMo8 is modeled and compared in the discussion [14]. Chromium 52100 steel was chosen for the cylindrical counterbody in order to maintain elastically similar conditions whilst simultaneously ensuring that cracks arose only in the plane specimens.

2.1. Contact configurations

A similar 2D cylinder/plane configuration was chosen both for plain fretting and fretting fatigue test experiments. The radius of the 52100 steel cylinder is R = 40 mm and the pad length L = 6 mm, giving plane strain conditions near the central axis of the fretting scar. Both AISI 1034 planes and fatigue specimens used respectively for plain fretting and fretting fatigue tests display a T=12 mm thickness. The normal load is fixed at $P=F_n/L= 227$ N/mm, inducing a maximum Hertzian pressure of p_{0H} = 450 MPa and a Hertzian contact half-width of a_H= 320 µm. In order to minimize edge-effects, the contact pad thickness and the transverse width of the plane specimen were machined to the same size. Hence, whilst the side faces of the contact are traction-free, approximate plane-strain conditions are present along the centerline of the contact. This means that the pressure distribution decreases from a maximum value along the central region to a lower value towards the contact ends, and eliminates any stress singularity problems [15]. Finally, the surfaces in contact were carefully polished to a mirror state (R_a around 0.05 µm).

2.3. Test conditions

As illustrated in Figure 3, two different test apparatuses were involved to quantify respectively the fretting and the fatigue influences in cracking processes.

Plain fretting test

The plain fretting stress conditions were achieved on a dedicated fretting wear test [16,17]. Fretting was applied by imposing a nominally static normal force (F_n= P.L), followed by a purely alternating cyclic displacement amplitude ($\delta*$), so that an alternating cyclic tangential load (F_t=Q*.L) was generated on the contact surface. During a test, F_n, F_t and δ were recorded, from which the δ - F_t fretting loop can be plotted; this cycle is characterized respectively by the tangential force (F_t) and slip displacement (δ*) amplitude. By analyzing the fretting loop, the sliding condition can be identified and the loading condition adjusted if necessary to maintain a partial slip contact configuration.

Fretting Fatigue test

The fretting fatigue apparatus is based on the conventional principle first introduced by the Oxford group [3] and successively developed by other research teams [5]. It consists of a hydraulic actuator imposing a fatigue loading on a fatigue specimen. A cylindrical pad is applied on one side of the fatigue specimen. Hence, contact loading is induced by the relative displacement between the fatigue specimen and the pad at the contact point. By adjusting the pad holder stiffness and/or the position of the contact along the fatigue specimen, it is possible to control the tangential contact loading with regard to the applied bulk stress. The tangential loading is determined either by strain gauges fixed on the pad holder apparatus, or by differential force measurements at each side of the fatigue specimen. Compared to classical setups, the LTDS system displays the following improvements [14]:

- A laser extensometer is adapted to measure the relative displacement between the pad and the fatigue specimen at the contact point. It allows the fretting loop to be plotted, which guarantees better control of the partial sliding condition,
- A dedicated system based on a ball bearing adjustment allows a single pad contact configuration to be implemented. The dispersion induced by contact misalignment and friction dispersion is reduced because only one contact needs to be adjusted. Besides, unlike the symmetrical configuration which requires a complex finite plate thickness correction, the whole specimen thickness can be considered for the stress analysis, which justifies the semi-infinite contact hypothesis.

- This fretting fatigue setup enables the application of a negative loading ratio. In the present investigation, all the tests were performed for alternated fatigue loading conditions (R=-1).

2.4. Identification of the friction coefficient at the sliding transition

Stress analysis of a fretting contact is highly dependent on the applied friction coefficient. Different approaches have been developed to determine this value [3, 18, 19]. A recent study shows that the friction coefficient measured at the transition between partial and gross slip conditions (μ_t) may be used to provide a representative value of the friction under partial slip conditions (i.e. $\mu_{PS} \approx \mu_t$) [20]. To determine the sliding transition, a variable displacement method was applied [20]. Several tests were performed, leading to $\mu_t = 0.85 \pm 0.05$.

3. Stress field analysis

The studied pressure condition is quite high compared to the yield stress of the material ($p_{0H}/\sigma y=1.28$). If a full sliding configuration is assumed, the very high friction coefficient will promote a generalized plastic deformation within the interface. However, because very small partial slip conditions are imposed, the plasticity is in fact constrained in narrow domains localized on the top surface sliding domains. Expecting plasticity to have a minor impact, we assume an elastic description of the contact and subsurface stress field distribution.

3.1. Plain fretting condition

The specimen thickness T=12 mm is defined so that each solid could be considered as an elastic half space, hence the solution for the pressure distribution is Hertzian [15, 21]. Similarly, the subsequent application of an alternating tangential force gives rise to a symmetrical shear traction distribution that is similar to that described by Mindlin and Deresciewicz [22]. A central stick zone ($|X| < c$) is bordered by regions of microslip. The contact half width, a, is small compared with the specimen thickness, T, ($a/T \approx 0.05$) so that no thickness correction [23] is needed.

The contact pressure contribution is assumed to be constant and static due to the very small displacement amplitude:

$$p(x)/a = \sqrt{1-(x/a)^2} \qquad (1)$$

The description of the cyclic shear contribution is more complex. It is defined as the superposition of different elliptic distributions to describe the pulsing evolution of the sliding front from the external contact border (a) to the inner stick boundary (c) where:

$$c = a \cdot \sqrt{1 - Q^*/(\mu.P)} \quad (2)$$

Hence, symmetrical shear stress field distributions are alternately imposed at the tangential force amplitudes +Q and –Q*.

3.2. Fretting Fatigue loading conditions

The elastic Fretting Fatigue stress description is developed using an on-phase Fretting - Fatigue loading condition. As shown by D. Nowell and al. [23], the bulk loading which is present in the fatigue specimen but not in the pad specimen promotes a mismatch in strains, giving rise to an additional term in the tangential matching. The result of the couple effect of fatigue loading on the partial fretting contact stress is the introduction of an "e" offset of the centre of the sticking zone from the centre of the contact. For the specific condition where e+c≤a, an explicit expression of the offset is available:

$$e = \frac{\sigma \cdot a}{4 \cdot \mu \cdot p_0} \quad (3)$$

Again, symmetrical shear stress field distributions are alternately imposed at tangential force amplitudes +Q and –Q* depending on the imposed bulk loading (Fig. 4).

By contrast to the plain fretting condition, the dissymmetry of the sliding distributions promotes a larger sliding domain at the trailing edge of the contact.

If larger bulk stresses are applied, (i.e. e+c > a), reverse slip takes place at one edge of the contact. Complex integral equations must then be solved to extract the shear stress field distribution.

Both fretting and fatigue loading are in phase and related to an alternating loading condition (stress ratio R=-1). The stress loading path can therefore be expressed by the two amplitude states, the so called loading and unloading conditions respectively (Fig. 4):

$$\Sigma_{loading} = \Sigma_{contact}(P,+Q^*) + \sigma_a$$

and

$$\Sigma_{unloading} = \Sigma_{contact}(P,-Q^*) - \sigma_a \quad (4)$$

The maximum loading state conditioning the crack nucleation risk and the crack propagation is located at the trailing edge (X=-1) at the loading condition.

3.3. Estimation of subsurface stresses induced by the contact loading

When the size of the contacting bodies is large compared to the contact size, a good approximation might be to consider each body as an elastic half-plane. With this approximation, once the surface stresses are known, the subsurface stresses induced by the contact loadings can be found by superposing half- plane Green's functions. For example, a general pressure distribution may be approximated in a piecewise-linear fashion by overlapping triangular elements [15]. The stresses at any general subsurface point for an individual element are provided by Johnson in [15] either for pressure or shear components. Thus, the full stress field due to a general stress distribution may be obtained from appropriate superposition of the simplified expressions mentioned. The full details of this numerical procedure and the limits of its application are provided by K. L Johnson [15] and D.A. Hills et al. in [21]. To reproduce as closely as possible the complex pressure and shear stress fields derived from the above interface analysis, the total number of increments is presently increased up to 2000, providing a lateral resolution equivalent to 1/1000 of the half contact width (i.e. triangular width of about 0.32 µm).

4. Quantification of the crack nucleation risk

4.1. Crossland's Multiaxial Fatigue Criterion

To predict the Fretting-Fatigue crack nucleation risk at the fatigue limit condition (i.e. 10^6 cycles), Crossland's multiaxial fatigue description is applied [24]. The crack risk is expressed as a linear combination of the maximum amplitude of the second invariant of the stress deviator ($\sqrt{J_2(t)}$) defined by ξ_a (Fig. 5), and the maximum value of the hydrostatic pressure ($P_{h\,max}$).

The non cracking condition is expressed by :

$$\xi_a + \alpha_C \cdot P_{h\,max} < \tau_d \tag{5}$$

Where

$$P_{h\,max} = \max_{t\in T}\left(\frac{1}{3}\,\mathrm{trace}(\Sigma(t))\right) \tag{6}$$

$$\xi_a = \frac{1}{2}\max_{t_0\in T}\left\{\max_{t\in T}\left[\frac{1}{2}(S(t)-S(t_0)) : (S(t)-S(t_0))\right]^{1/2}\right\} \tag{7}$$

$$\alpha_C = \frac{\tau_d - \sigma_d/\sqrt{3}}{\sigma_d/3} \quad (8)$$

with,

S : deviatoric part of Σ

σ_d : alternating bending fatigue limit,

τ_d : alternating shear fatigue limit.

The cracking risk can then be quantified through a scalar variable:

$$d_C = \frac{\xi_a}{\tau_d - \alpha_C \cdot P_{h\,max}} \quad (9)$$

The cracking condition is then expressed as:

- If d_C is greater than or equal to 1, there is a risk of cracking;

- If d_C remains less than 1, there is no risk of cracking.

4.2 Calibrating the crack nucleation prediction on plain fretting conditions

The first step of the methodology is to calibrate the model by iterating the experimental crack nucleation limit defined from plain fretting tests. To identify the experimental crack nucleation threshold, the following procedure is applied:

Keeping the pressure and the test duration constant, various tests are performed at different tangential force amplitudes. In the present investigation we focus on high cycle endurance conditions so we consider that the crack nucleation limit is reached at 10^6 cycles. Cross-sections at different places along the median axis of the fretting scars are then taken. The maximum crack lengths observed are plotted versus the applied tangential force amplitude (Table 2). A linear approximation can be considered (Fig. 6).

The crack nucleation condition is usually defined for an arbitrary crack length. Depending on the crack length, different crack nucleation thresholds might be considered, which complicates the crack nucleation analysis. This paradox is here resolved by defining the crack nucleation threshold as the limit tangential force amplitude (Q^*_{CN}) below which no crack can be observed (b=0). To determine this value, the following strategy is applied: assuming a linear evolution of the crack length versus the tangential force amplitude, we extrapolate the crack nucleation threshold (Q^*_{CN}) when this linear extrapolation crosses the X axis (i.e. crack length b = 0 µm). To confirm this value, few tests are then performed just below this

extrapolated value to verify that no cracks have nucleated. For the studied condition we determine Q^{*}_{CN} = 100 N/mm (Fig. 6).

The multiaxial fatigue analysis is then performed for the threshold crack nucleation condition. Confirming the experiments, figure 7 shows that the maximum crack risk is located at the contact borders, but the computed value d_C is around 2. As mentioned previously, the current point stress analysis critically over-estimates the cracking risk. Indeed, the cracking risk analysis under severe stress gradient conditions requires that more representative averaged stress states defined over intrinsic length scales be considered [6, 7].

A pertinent cracking risk analysis will consist first in identifying a representative stress state, taking into account the stress gradient (Σ_R), then in applying a multiaxial fatigue analysis. Taylor et al. [25] have extensively investigated this aspect, focusing on the peculiar stress gradient generated by notch discontinuities but considering a crack propagation approach. We adopt the Taylor strategy, considering a multidimensional approach to identify representative stress states (Fig. 8).

Crack nucleation process volume (3D averaging approach)

First introduced in Fretting problems [6], it consists in establishing a representative loading state by averaging the stress state over a 3D representative "crack nucleation process volume". The point stress analysis is replaced by a mean loading state $\overline{\Sigma}(M)$ averaged over the micro volume V(M) surrounding the point on which the fatigue analysis is performed (M (x,y)) (Fig. 8) [6]. This micro volume of matter is approximated through a cubic volume, whose edges are assimilated to the physical length scale ' ℓ_{3D} '. For the studied 2D plain strain configuration, the volume stress state analysis is reduced to a surface area averaging. The "3D" representative stress state is therefore expressed through the following expression:

$$\Sigma_{R3D}(x,y) = \overline{\Sigma}(V(M(x,y),\ell_{3D})) = \frac{1}{25}\cdot\sum_{i,j=-2}^{2}\Sigma(M(x+i\cdot\frac{\ell_{3D}}{4}, y+j\cdot\frac{\ell_{3D}}{4})) \quad (10)$$

Crack nucleation process surface (2D averaging approach)

A crack displays a planar morphology so there is a physical justification to consider a plane averaging procedure rather than a volume approach. Indeed, although it is simpler to implement, a volume averaging procedure involves out-plane stress components and therefore can induce discrepancy. The "2D" representative stress state can be approximated by the mean loading state averaged over a square area, whose edges are assimilated to the physical

length "ℓ_{2D}". In fretting fatigue problems, a crack nucleates at the surface trailing edge of the contact and usually propagates perpendicularly to the fatigue loading. The square area can therefore be assumed to be normal to the surface and the fatigue directions with one edge located on the top surface. For the studied 2D plain strain configuration, the analysis is reduced to a "y" line averaging procedure (Fig. 7).

The following formulation is hereafter considered:

$$\Sigma_{R2D}(x) = \overline{\Sigma}(L(M(x, y=0), \ell_{2D})) = \frac{1}{5} \cdot \sum_{i=0}^{4} \Sigma(M(x, i \cdot \frac{\ell_{2D}}{4})) \quad (11)$$

Critical distance method

This method is equivalent to the point stress analysis and does not involve an averaging procedure. However, rather than consider the surface stress discontinuity to predict the cracking risk, fatigue analysis is performed from a stress state defined below the surface at a critical distance called "ℓ_{1D}". Like for the averaging procedures, this infers a significant reduction of the maximum loading state and therefore, a better integration of the stress gradient effect. For the studied 2D cylinder plane configuration, the surface representative stress state related to the contact surface is expressed by the following expression:

$$\Sigma_{R1D}(x) = \Sigma(M(x, y=\ell_{1D})) \quad (12)$$

Different methodologies can be applied to extrapolate the former length scale parameters. Some approaches consider the crack length marking the transition from short to long crack propagation regime; others are based on grain size. In the present investigation, we adopt a reverse identification methodology involving iterative procedures to extrapolate the optimized length values predicting the experimental plain fretting crack nucleation condition (i.e. p_{0H} = 450 MPa, a_H= 320 µm, μ_t=0.85, Q^*_{CN} = 100 N/mm) [6,17]. Figure 9 illustrates this methodology by plotting the evolution of the predicted cracking risk as a function of the 3D length scale parameter (i.e. process volume approach). A pertinent prediction of the cracking risk is found for $\ell_{3D\_Crossland}$ = 45 µm. This dimension is very close to the Austenite grain size of the AISI 1034 alloy, which supports the hypothesis of a correlation between the length scale parameter and the microstructure [6]. The reverse identification methodology is then applied to identify the length scale parameters related to the crack nucleation process surface and the critical distance methods. We determine $\ell_{2D\_Crossland}$ = 55 µm and $\ell_{1D\_Crossland}$ = 20

µm respectively. These results are consistent with Taylor et al.'s conclusions which suggest a constant correlation between the various length scale parameters ($\ell_{3D} \approx \ell_{2D} \approx \ell_{1D}/2$).

4.3. Predicting the crack nucleation risk under Fretting-Fatigue loading conditions

To establish the experimental crack nucleation boundary under Fretting-Fatigue conditions, the following methodology was applied. Three fatigue stress levels were defined. For each fatigue level, different tests were performed, adjusting the fretting tangential force amplitude by monitoring the test apparatus stiffness. Like for plain fretting investigations, the test duration was fixed at 10^6 cycles. After the test, cross section observations were performed to see if any cracks had been activated. The studied loading conditions are compiled in table 3.

Figure 10 plots the experimental damage as a function of the imposed fretting and fatigue loading conditions defining the so-called Crack Nucleation Fretting Fatigue Map (CN-FFM). The experimental crack nucleation boundary is estimated by separating both cracking and non cracking domains. It is characterized by an initial sharp decrease followed by a quasi constant evolution. Hence, the threshold crack nucleation boundary stabilizes at 80% of the plain fretting condition in the middle fatigue stress range (i.e. σ_a/σ_d <0.5). The application of a fatigue bulk stress decreases the admissible fretting loading. However, its influence appears less effective than expected. This suggests that for the studied medium-low fatigue stress range (i.e. σ_a/σ_d <0.5), the crack nucleation process is mainly controlled by the contact loading. Further experiments are now required to investigate the crack nucleation process in the high fatigue stress region (i.e. $\sigma a/\sigma d$<0.5) in order to see until which fatigue stress condition the influence of the contact predominates, and how the crack nucleation boundary converges toward the fatigue limit σ_a/σ_d =1).

Comparison between stress averaging methods

To formalize the crack nucleation boundary, the multiaxial Crossland fatigue criterion is applied and the different length scale approaches compared. As expected, the conventional point stress analysis clearly underestimates the safe crack nucleation domain (Fig. 10). It shows an asymptotic decrease from the plain fretting condition (i.e. $Q^*/\mu P$=0.18) to zero at the fatigue limit (i.e. σ_a/σ_d =1.0). This convergence toward a zero tangential loading is consistent with the fact that the stress state at the contact borders defined from the point stress methodology is dependent on the tangential force only. Therefore, when the bulk loading reaches the fatigue limit, the threshold tangential force amplitude is obviously equal to zero.

The length scale approaches (i.e. crack nucleation process volume, crack nucleation process surface and critical distance method), display quasi superimposed evolutions which suggests that, apart from numerical implementation considerations, none of them can be preferred to describe the stress gradient effect induced by fretting loading.

They show a quasi linear decrease of the admissible tangential loading from the plain fretting condition down to a small residual positive value when $\sigma_a/\sigma_d=1$. This residual tangential force, estimated near $Q^*/\mu P=0.05$, is in fact required to compensate for the compressive stress state induced by the static normal component. Unlike the point stress analysis, length scale approaches consider a loading region where the mean stress level controlled by the normal loading is not zero but compressive. This suggests that for low fretting and high fatigue loading conditions, crack nucleation could be observed outside the contact region. Such a peculiar situation has been confirmed in different experimental investigations, and indirectly supports the applied length scale descriptions to quantify the crack nucleation risk under fretting fatigue conditions.

The length scale approaches are clearly more realistic than the conventional point stress to predict the safe crack nucleation domain. However the predictions are still uncertain:

- They provide a very good description of the crack nucleation process for the low fatigue stress range (i.e. $\sigma_a/\sigma_d <0.1$),
- Within the intermediate fatigue stress domain (i.e. $0.1<\sigma_a/\sigma_d<0.5$), the length scale approaches predict a quasi-linear decrease of the crack nucleation boundary, whereas experiments conclude that the admissible fretting loading stabilizes. The higher the bulk stress, the larger the discrepancy with the models.
- Convergence is however expected for the higher fatigue stress range ($0.5<\sigma_a/\sigma_d <1.0$), which unfortunately cannot be addressed in the present investigation due to technical limitations. Indeed, due to high compressive stress levels, the experimental results have been corrupted by buckling instabilities of fatigue specimens. Current developments allowing shorter Fretting-Fatigue specimen configurations are expected to solve this limitation.

Comparison between multiaxial fatigue criteria

To verify if the discrepancy observed for the intermediate fatigue stress domain could be explained by crack nucleation formulations, other descriptions like Dang Van [26] and McDiarmid [27] criteria are compared. The given strategy consisting in calibrating the representative process volume using the threshold plain fretting cracking condition (i.e. p_{0H} =

450 MPa, a_H= 320 µm, μ_t=0.85, Q^*_{CN} = 100 N/mm) is here applied [28]. We deduce respectively: $\ell_{3D\_DangVan}$ = 60 µm and $\ell_{3D\_McDiarmid}$ = 95 µm.

Figure 11 confirms similar evolutions between the multixial fatigue criteria and equivalent dispersion versus the experiments. It shows that whatever the multiaxial fatigue formulations, the stress gradient calibration from plain fretting condition systematically provides pessimistic estimations of crack nucleation boundaries. Moreover, the very small difference between the fatigue criteria suggests that the fretting-fatigue stress condition, characterized by a "quasi" bi-axial stress state, is not appropriate to discriminate between the former multiaxial formulations.

The present investigation clearly demonstrates that the discrepancy between the experimental crack nucleation boundary and multiaxial modeling is not related to the length scale averaging procedure or the fatigue crack nucleation formulation. Alternative hypotheses must be considered, like plasticity, which interacts with the stress distribution and introduces local residual stresses, or the current length scale methods which are established from fixed length values but could be optimized by considering variable length scale dimensions as a function of the stress gradient fluctuations.

However, one important conclusion of this work is the fact that a multiaxial fatigue analysis combined with a length scale approach calibrated from plain fretting conditions enables a conservative approximation of the crack nucleation boundary under fretting fatigue loadings. Due to its capacity to be generalized for any stress configurations like subsurface stress discontinuities, the crack nucleation process volume approach combined with the simple Crossland formulation will be preferred and applied in the following development.

5. Quantification of the crack propagation risk

5.1. Determining the Stress Intensity Factor (SIF)

Crack tip stress intensity factors have been found using the distributed dislocation method which is described in detail in [29]. The technique employs Bueckner's principle [30] which is simply an elastic superposition principle. Suppose a cracked body is subjected to a varying stress field like that imposed by a fretting fatigue (Fig. 12). A problem equivalent to the original would be the superposition of the body without a crack subjected to the external fretting fatigue load (A) and a cracked body devoid of external loads but whose crack line traction and shear are equal and opposite to the stress components along the line of the crack

(B), so that after summing the two (A+B) the crack faces are traction-free. Note that by taking this approach we are implicitly making the assumption that the effect of the crack on surface displacements is small, so that surface stresses remain unchanged by the presence of the crack. A simplified single crack initiated at the contact trailing edge (X=x/a=-1), and normal to the surface is considered (Fig. 12). Note this assumption has been extensively considered in many Fretting-Fatigue investigations and was confirmed by examination of the cracking damage.

The stress components along the crack face are collected in order to determine the unsatisfied tractions (σ_N, σ_S). Since the crack faces have to be traction free, we distribute both climb and glide displacement discontinuities (or "dislocations") along the crack so that the stresses induced ($\tilde{\sigma}_{yy}, \tilde{\sigma}_{xy}$) cancel σ_N and σ_S. The integral equations expressing the requirement that the crack faces be traction free are:

$$\sigma_S(\hat{x}) + \frac{G}{4\pi(\nu+1)}\left\{\int_0^b B_{\hat{x}}(e)K_{\hat{x}}^S(\hat{x},e)\,de + \int_0^b B_{\hat{y}}(e)K_{\hat{y}}^S(\hat{x},e)\,de\right\} = 0$$

$$\sigma_N(\hat{x}) + \frac{2G}{4\pi(\nu+1)}\left\{\int_0^b B_{\hat{x}}(e)K_{\hat{x}}^N(\hat{x},e)\,de + \int_0^b B_{\hat{y}}(e)K_{\hat{y}}^N(\hat{x},e)\,de\right\} = 0 \qquad (13)$$

with G and ν the shear modulus and the Poisson coefficients.

Where $\sigma_S(\hat{x})$ and $\sigma_N(\hat{x})$ are the resolved shear and normal components of the stress tensor $\sigma(x,y)$ in the $(\hat{x},\hat{y})$ coordinate of the system, $K_{\hat{x}}^N$, $K_{\hat{y}}^N, K_{\hat{x}}^S$, $K_{\hat{y}}^S$ are the kernels established by the above method detailed in [29, 31].

It is not possible to solve the equation analytically, but powerful numerical quadratures are given in references [29, 31]. The dislocation densities $B_{\hat{x}}$ and $B_{\hat{y}}$ are determined and the stress intensity factor K_I and K_{II} at the crack tip are successively approximated using a Krenk's interpolation [29]. Full details of the numerical procedure are given by Nowell and Hills in [29]. We should recognize that the approach we have followed is purely elastic, whereas in practice some plasticity may be present.

5.2. Definition of an effective stress-intensity range parameter

The crack propagation analysis requires the determination of a pertinent effective stress-intensity range parameter (ΔK_{eff}). This latter is not easy to determine, particularly under complex and high stress gradient conditions like imposed by fretting fatigue loading. The

adopted strategy will consist to consider different formulations to estimate ΔK_{eff} and to compare the experimental crack arrest conditions. The best fitting will permit us to establish the most relevant ΔK_{eff} assumption. It has been shown that contact loading induces a mixed mode stress condition [32]. Therefore the following hypotheses will be considered to quantify cracking behaviors:

A – Mixed mode taking into account the full loading range

The full range of mode I and mode II contributions are considered. The effective stress range is expressed by :

$$\Delta K_{eff\_A} = \sqrt{\Delta K_I^2 + \Delta K_{II}^2} \quad (14)$$

with $\Delta K_{II} = K_{II\,max} - K_{II\,min}$ and $\Delta K_I = K_{I\,max} - K_{I\,min}$ (15)

where $K_{II\,max}$ is defined at the loading state when $K_I = K_{Imax}$ (i.e. open crack condition) and $K_{II\,min}$ computed at the unloading state (i.e. Q=-Q*, $\sigma_{FATIGUE} = -\sigma_a$ and $K_I = K_{Imin}$ inducing a closed crack situation (Fig. 4). This formulation, neglecting both closure and crack face friction effect, provides an upper bound estimation of the effect stress-intensity range parameter (ΔK_{eff}) and therefore a pessimist estimation of the crack arrest condition (i.e. smaller predicted crack arrest domain).

B – Mixed mode taking into account the closure effect but neglecting crack face friction

Because pure alternating loading conditions are imposed (R = -1), the usual Elber's assumption that the effective mode I stress intensity range can be reduced to the maximum stress intensity value (i.e. $\Delta K_{Ieff} = K_{I\,max}$) is considered [14]. The mode II contribution is considered with the implicit assumption that crack face friction is negligible (i.e. that mode II loading of the crack is unaffected by contact with the crack faces). We deduce :

$$\Delta K_{eff\_B} = \sqrt{K_{Imax}^2 + \Delta K_{II}^2} \quad (16)$$

with $\Delta K_{IIeff} = K_{II\,max} - K_{II\,min}$ (17)

C – Mixed mode taking into account the closure effect and crack face friction

Many investigations confirm that friction phenomena within the crack interface, reduce the mode II contribution. One approximation is to neglect the mode II contribution when the

crack faces are under compression state (i.e. at the unloading state). The effective SIF range is therefore estimated by:

$$\Delta K_{eff\_C} = \sqrt{K_{I\max}^2 + K_{II\max}^2} \quad (18)$$

D - Pure mode I

The mode II contribution is neglected and the effective stress intensity range is identical to the mode I component:

$$\Delta K_{eff\_D} = K_{I\max} \quad (19)$$

where $K_{I\max}$ is defined at the loading state (i.e. Q=+Q* and $\sigma_{FATIGUE}=+\sigma_a$).

5.3. Short crack methodology

The examination of the crack suggests that crack propagation may take place in the short crack regime when the actual stress intensity factor range is less than the long crack threshold, ΔK_0. We therefore intend to apply short crack approaches, to predict the crack arrest conditions. Two strategies are here considered. The first, based on the Kitagawa and Takahashi diagram, consists in a discontinuous description of the transition from short to long crack domains and the second, introduced by El Haddad and co-authors [12] considers a smooth continuous transition.

5.3.1 K-T's threshold of the short crack arrest condition

First introduced by Araujo et al. for fretting fatigue conditions [10], the starting point of this approximation is based on the Kitagawa and Takahashi diagram [11] which shows that small cracks can propagate at $\Delta K < \Delta K_0$ provided that the stress is high enough.

We choose to examine the propagation of the crack in the *modified* K-T diagram (i.e. where ΔK rather than stress is plotted against *b*) (Fig. 13). Hence, the threshold SIF range related to the crack arrest condition (ΔK_{th}) is given by

$$\Delta K_{th} = \Delta K_0 \cdot \sqrt{\frac{b}{b_0}} \qquad \text{if } b \le b_0 \text{ (small crack)} \quad (20)$$

$$\Delta K_{th} = \Delta K_0 \qquad \text{if } b > b_0 \text{ (long crack)} \quad (21)$$

Where b_0 , is the transition crack length between short and long crack regimes, approximated by :

$$b_0 = \frac{1}{\pi} \cdot \left(\frac{\Delta K_0}{1.12 \cdot \sigma_d} \right)^2 \quad (22)$$

For the alloy used here, this gives b_0 = 170 µm (since ΔK_0 = 7 MPa√m). The crack arrest condition is assumed when the following inequation is satisfied:

$$\Delta K_{eff} \leq \Delta K_{th} . \quad (23)$$

5.3.2 El Haddad's threshold of the short crack arrest condition

Like for the previous description, the transition from short to long crack behavior is related to the threshold crack length b_0. However, rather than considering a discontinuous transition, we assume the continuous El Haddad approximation of the short crack arrest threshold (Fig. 13):

$$\Delta K_{th} = \Delta K_0 \cdot \sqrt{\frac{b}{b + b_0}} \quad (24)$$

Figure 13 confirms that whatever the crack length, El Haddad's approximation provides a lower value of the threshold crack arrest condition. The difference is particularly important in the transient domain when b= b_0. This suggests that El Haddad's approximation is more conservative than K-T's approach.

5.4. Predicting the crack arrest condition under Fretting-Fatigue loading conditions

To establish the experimental crack arrest boundary, the following methodology has been defined. Three levels of fretting loading have been selected, respectively Q*/µP=0.5, 0.63 and 0.73. For each contact loading, the alternated fatigue stressing was adjusted from σ_a/σ_d= 0.4 to 0.6. The studied loading conditions selected above the crack nucleation boundary and the corresponding damage evolutions are reported in Table 4.

By contrast with the nucleation phenomenon, propagation failure can be observed after several million cycles. Therefore, to estimate the stabilized crack arrest conditions, the test duration was increased up to 10 million cycles. Hence, for each test, cracking damage is characterized by reporting either if the specimen is broken after 10^7 cycles or if the maximum crack length for unbroken specimens is found. All the experimental results are reported in Figure 14, defining the so-called Crack Arrest Fretting Fatigue Map (CA-FFM). Like for the crack nucleation analysis, the experimental crack arrest boundary can be extrapolated from failure and non-failure conditions. The experimental crack arrest boundary displays a quasi

vertical evolution, which suggests that the crack arrest process is only a function of the fatigue loading and relatively unaffected by contact stress. This result confirms the conventional idea that under fretting-fatigue, crack nucleation is controlled by contact loading, whereas crack arrest is mainly controlled by fatigue bulk stressing. This conclusion is however restricted to the medium fatigue stress range ($0.4 < \sigma_a/\sigma_d < 0.6$) and must be tempered regarding the relative contact size and the small loading range studied.

As described previously, crack modeling was carried out assuming a single crack normal to the surface and located at the trailing edge (X=-1), where the maximum value of crack nucleation risk has been found. Then, for each fretting loading condition, the modeling strategy consists in identifying, by iterative computations, the maximum fatigue stressing below which the crack arrest condition is achieved. This analysis is applied for the different approximations of the effective SIF range parameters and the two short crack arrest approaches.

Comparison with the models suggests that the mixed mode taking into account the full loading range (ΔK_{eff_A}) is too pessimistic whatever the short crack arrest approximation. By contrast, pure mode I (ΔK_{eff_D}) but also the mixed mode taking into account the closure effect and the crack face friction (ΔK_{eff_C}) approximations are too optimistic. Both ΔK_{eff_D} and ΔK_{eff_C} formulations display a quasi superimposed evolution which infers that the mode II contribution during the loading step (i.e. $K_{II\,max}$) is quasi negligible.

The best approximation of the experimental crack arrest boundary is achieved by combining both the mixed mode, taking into account the closure effect but neglecting the crack face friction (ΔK_{eff_B}), and Haddad's approximation of the short crack arrest condition.

All the failure conditions are predicted. The model is even able to discriminate between the non-failure condition (FF12) and the failure situation (FF15), which are characterized by a fatigue stress difference of less than 10 MPa. This investigation also suggests that a plain mode I description and K-T's approximation can induce dangerous optimistic crack arrest predictions. The better approximation of the crack arrest condition provided by Haddad's approximation is confirmed in Figure 15, where the maximum crack length at the crack arrest condition is plotted versus the corresponding effective SIF range value (ΔK_{eff_B}).

K.T.'s approximation provides a rather good estimation of the crack arrest condition in the short crack arrest domain (i.e. $b<b_0$) but unfortunately appears too optimistic in the intermediate short / long crack domain. El Haddad's approximation, providing a smoother

evolution toward the long crack domain, leads to a more conservative prediction of the crack arrest condition (Fig. 14 and 15).

A significant discrepancy between the experimental crack arrest boundary and the safe El Haddad – mixed mode approximation is nevertheless still observed. This infers that more elaborated formulations, taking into account plasticity, closure and representative friction effects in the crack faces should be introduced into the model. Besides, more complete short crack arrest descriptions have to be considered for future optimization of the modeling. Moreover, the practical difficulties which are experienced in obtaining an experimental value for the long crack threshold must be underlined. Perhaps a better estimation of this value combined with an optimized description of the effective stress intensity factor can allow the application of the less conservative KT's formulation, as can be expected from Figure 15 which shows that only one experimental point is below KT's boundary. However, some cautions need to be exercised regarding KT's approximation. Figure 14a, shows that two specimen failures are not predicted by it.

The main objective of this work is to provide realistic and safe estimations of the cracking response. Therefore, in spite of its limitations, the current pessimist strategy which combines an El Haddad description of the short crack arrest condition, an elastic description of the stress field and the application of a mixed-mode formulation taking into account the closure effect but neglecting the crack face friction appears to be a good compromise to approximate the crack arrest boundary in the CA-FFM initially.

6. Synthesis

6.1 Impact of material properties

Both crack nucleation and crack arrest boundaries are reported on the same graph, defining the so called Material Response Fretting-Fatigue Map (Fig. 16). The experimental results are compared respectively with the model of crack nucleation defined from Crossland's multiaxial fatigue criterion, by taking into account the stress gradient effect through a 3D process volume description, and using the crack arrest boundary defined from the El Haddad-mixed mode approximation (ΔK_{eff_B}).

The studied alloy displays a comparatively low fatigue limit but a high crack arrest threshold. This implies a rather small safe crack nucleation domain but a large crack arrest domain. Hence, for this specific alloy, the safe crack nucleation domain is systematically bordered by the crack arrest domain (Fig. 16). This favors a conservative prediction of cracking risk.

Indeed, assuming a loading state located in the safe crack nucleation domain, even if a crack is accidentally nucleated, the structure will be safe because the crack is expected to be stopped whatever the fatigue stress applied (i.e. $\sigma_a < \sigma_d$).

Materials displaying an elevated fatigue limit but low damage tolerance are more complex to interpret. Figure 17 plots the estimated crack nucleation and crack arrest boundaries for an equivalent loading spectrum (i.e. similar contact and fatigue loading ranges) but considering a 30NiCrMo8 low-alloy steel whose estimated fatigue properties are respectively σ_d(R=-1) = 420 ±10 MPa and $\Delta K_0 = 4 \pm 1$ MPa$\sqrt{m}$ (Table 1)[14]. Applying relation (22) we deduce a very short long crack length transition around b_0 = 23µm. This alloy is characterized by a tempered Martenstic structure displaying an original Austenitic grain size around 10µm diameter. The latter dimension is currently adopted for the stress averaging analysis (i.e. $\ell_{3D} = 10\ \mu m$), which, combined with Crossland's multixial fatigue formulation, allows us to estimate the crack nucleation boundary.

Compared to the AISI 1034 steel (Fig. 16), the safe crack nucleation domain is increased but not as expected (Fig. 17). Indeed, the fatigue limit of the 30NiCrMo8 alloy is significantly higher but the process volume applied is smaller, which reduces the stress averaging effect; therefore the crack nucleation boundary remains quasi unchanged.

Simultaneously, the sharp reduction of the long crack threshold (ΔK_0) promotes a severe reduction the crack arrest domain. It is interesting to note that above a given bulk stress (σ_{a_CAth}), the so called Fretting–Fatigue Crack Arrest Bulk Stress Limit, the crack arrest boundary passes below the crack nucleation boundary. Therefore, above this bulk stress limit, if a crack nucleates, it will systematically propagate until failure because the intermediate crack arrest domain no longer exists. Hence, by contrast to the lower fatigue loading range ($\sigma_a < \sigma_{a\_CAth}$) or the application of damage tolerant materials like AISI 1034 steel, such a contact configuration is greatly corrupts the stability and the safety of a cracking risk design based on a safe crack nucleation approach. Higher security factors, to reduce cracking risk, are required.

Figure 18 compares the global response of the two alloys. The upper limits between the crack nucleation and crack arrest boundary are plotted as a function of the applied fretting and fatigue loadings. The upper limit of safe cracking damage systematically corresponds to the crack arrest boundary for the AISI 1034 steel but alternatively to the crack arrest or the crack nucleation limits, for the 30NiCrMo8 alloy, depending on whether the fatigue stress is above

or below σ_{a_CAth}. One important conclusion is that, despite its very low mechanical properties, the AISI 1034 steel alloy appears more resistant against fretting fatigue cracking due to higher damage tolerance properties (i.e. higher crack threshold (ΔK_0)).

6.2 Fretting Fatigue Palliatives

In the previous paragraph, the link between the fatigue properties of the bulk material and the Fretting-Fatigue cracking evolution was discussed. However, in most fretting problems, surface palliatives are usually applied to reduce the cracking risk [33]. A first approach consists is to drastically reduce the coefficient of friction and consequently the cyclic fretting stresses. However, in many assemblies, a medium friction value is required to keep fixed the contact. Specific surface treatments are therefore required to prevent the crack nucleation process. This can be achieved using thin hard coatings, like PVD TiN coating, which induces very high and stable compressive stresses, and so can definitively block the surface crack nucleation process [33]. Crack nucleation can also be avoided by applying thick coatings like CuNiIn or WC-Co layers using plasma or HVOF technologies (Fig. 19). The top surface fretting stresses are fully accommodated by the layer, and the bulk material is then protected from crack nucleation.

A second strategy is to apply an in-depth surface treatment to limit and even block crack propagation (Fig. 19). Shot peening and laser peening are the most common treatments of this category. Compressive residual stresses deep below the surface are introduced by the application of plastic deformations. By contrast to conversion treatments or thin hard coatings, these compressive stresses are not stable, and, when a cyclic loading give beyond the plastic yield, the compressive residual stresses are partly or fully erased. Fretting loading tends to relax the surface compressive stresses and explains why it is usually admitted that shot peening treatment does not improve the crack nucleation response of a fretting fatigue contact (Fig. 19a). However, below the surface, where contact stress reduces, the residual compressive stresses are maintained and will play a determining part in blocking crack propagation, inducing a sharp increase of the fretting fatigue limit (Fig. 19b). For critical systems, these two palliative strategies are combined (Fig. 19) either to extend the crack nucleation domain by applying a thick coating like WC-Co HVOF layers, or to increase the crack propagation resistance by introducing a very deep residual compressive stress field using shot peening and now laser peening.

As illustrated in Figure 20, the given Fretting-Fatigue Mapping concept appears as a useful approach to quantify and compare the relative benefits of palliative strategies against fretting fatigue damage. Surface crack nucleation palliatives, by improving crack nucleation resistance, obviously extend the safe crack nucleation domain but also promote a shift of σ_{a_CAth} towards lower fatigue stresses, and consequently induce a reduction of the intermediate crack arrest domain (Fig. 20a). Surface treatments improving the crack propagation resistance extend the intermediate crack arrest domain and consequently increase the threshold value σ_{a_CAth} (Fig. 20b). Combined safe crack nucleation and crack arrest palliatives extend both safe crack nucleation and crack arrest domains, and smoothly shift the threshold stress σ_{a_CAth} toward highest fatigue stress values (Fig. 20c).

7. Conclusion

An experimental methodology has been developed to identify, respectively, crack nucleation and crack arrest conditions as a function of the applied fretting and fatigue loadings. Synthetic Fretting Fatigue maps have been introduced, defining respectively, the safe crack nucleation, crack arrest and catastrophic failure material responses. It is shown that a basic elastic approximation of the fretting-fatigue loading combined with a Crossland multiaxial fatigue analysis is able to predict the crack nucleation boundary if the contact stress gradient effect is taken into account. This can be achieved by using a process volume methodology, where the stress state considered for the multiaxial fatigue analysis is averaged over a representative volume. It has also been shown, that for the peculiar stress gradient imposed by a contact fretting loading, the different stress averaging approaches like the 3D stress process volume, the 2D stress process surface, and the critical distance method converge to similar results. This work shows that the process volume approach can be calibrated by using plain fretting tests, and extrapolated to more complex fretting fatigue configurations providing a conservative prediction of the crack nucleation risk. Alternative multiaxial fatigue criteria like Dang Van and McDiarmid formulations lead to similar conclusions, suggesting the “over-conservative” prediction in the medium fatigue stress range is not related to the fatigue criterion formulation but seems to depend on the stress averaging strategy. Hence more advanced stress averaging approaches must be considered if more realistic but less conservative predictions of the crack nucleation boundary are required.

It is also shown that a plain El Haddad short crack arrest methodology combined with a mixed mode SIF approximation allows a conservative description of the crack arrest domain. Based on these different approximations, Material Response Fretting Fatigue maps of various alloys can be compared. Taking into account the material properties and the applied contact configuration, different palliative strategies (i.e. surface treatments) can then be adopted, focusing either on crack arrest or safe crack nucleation strategies.

References

[1] Hoeppner DW, Chandrasekaran V, Elliot CB, editors. Fretting fatigue: current technology and practices; ASTM STP 1367, American Society for Testing and Materials, 2000, ISBN 0-8031-2851-7.

[2] Waterhouse, R.B., Fretting Fatigue, Applied Science publishers, 1981.

[3] Hills DA, Nowell D. Mechanics of fretting fatigue, Dordrecht: Kluwer Academic Publishers, 1994.

[4] Fouvry S., Kapsa Ph., Vincent L., Dang Van K. Theoretical analysis of fatigue cracking under dry friction for fretting loading conditions. Wear 1996;195:21-34.

[5] Szolwinski, M.P., Farris, T.N. Mechanics of fretting crack formation. Wear 1996;198: 93-107.

[6] Fouvry S, Kapsa Ph, Sidoroff F, Vincent L. Identification of the characteristic length scale for fatigue cracking in fretting contacts. J. Phys. IV France 1998; 8: 159-166.

[7] Araújo JA, Nowell D. The effect of rapidly varying contact stress fields on fretting fatigue. International Journal of Fatigue 2002; 24 (7): 763-775.

[8] Giannakopoulos AE, Lindley TC, Suresh S, Chenut C. Similarities of stress concentrations in contact at round punches and fatigue in notches: implications to fretting fatigue crack initiation. Fatigue and Fracture of Engineering Materials and Structures 2000;23:562–71.

[9] Mugadu A, Hills DA, Barber JR, Sackfield A. The application of asymptotic solutions to characterising the process zone in almost complete frictional contacts. International Journal of Solids and Structures 2004; 41 (2):385-397.

[10] Araújo JA, Nowell D. Analysis of pad size effects in fretting fatigue using short crack arrest methodology, International Journal of Fatigue 1999;21:947-956.

[11] Kitagawa H, Takahashi S. Application of fracture mechanics to very small cracks or the cracks in the early stage. Philadelphia: American Society for Metals, 1976:627-630.

[12] El Haddad MH, Smith KN, Topper TH. Fatigue crack propagation of short cracks. Journal of Engineering Materials and Technology 1979;101:42-46.

[13] Gros V. Etude de l'amorçage et de la propagation des fissures de fatigue dans les essieux-axes ferroviaires, D. Phil. Thesis, Ecole Centrale de Paris, France,1996.

[14] Kubiak K., Fouvry S., Marechal A.M., Vernet J.M. Behaviour of shot peening combined with WC–Co HVOF coating under complex fretting wear and fretting fatigue loading conditions. Surface and Coatings Technology 2006; 201(7):4323-4328.

[15] Johnson KL., Contact Mechanics, Cambridge University Press,1985.

[16] Zhou Z. R., Vincent L. Mixed fretting regime. Wear 1995;181-183(2):531-536.

[17] Fouvry S, Duo P, Perruchaut Ph. A quantitative approach of Ti-6Al-4V fretting damage: Friction, Wear and crack nucleation. Wear 2004; 257(9-10): 916-929.

[18] Fouvry S., Kapsa Ph., Vincent L. Developments of fretting sliding criteria to quantify the local friction coefficient evolution under partial slip condition. Tribology Series1998; 34:161-172.

[19] Dini, D. Nowell D. Prediction of the slip zone friction coefficient in flat and rounded contact Wear. 2003;254 (3-4):64-369.

[20] Proudhon H., Fouvry S., Buffière J.-Y. A fretting crack initiation prediction taking into account the surface roughness and the crack nucleation process volume. International Journal of Fatigue,2005; 27(5):569-579.

[21] Hills, D.A., Nowell, D., Sackfield, A. Mechanics of Elastic Contacts, Oxford Butterworth- Heinemann , 1993.

[22] Mindlin RD, Deresciewicz H. Elastic sphere in contact under varying oblique forces. J Appl Mech 1953, 75:327-344.

[23] Nowell, D., Hills, D.A., Mechanics of Fretting Fatigue tests. Int. Jnl. Mech. Sci. 1987;29(5):355-365.

[24] Crossland B. Effect of large hydrostatic pressures on the torsional fatigue strength of an alloy steel. Proceeding of the Inter. Conf. On Fatigue of Metals, Inst. of Mechanical Engineers, London, 1956, pp. 138-149.

[25] Taylor D. Geometrical effects in fatigue: a unifying theoretical model. International Journal of Fatigue 1999; 21:413-420.

[26] Dang Van K. Macro-micro approach in high-cycle multiaxial fatigue. ASTM 1993; STP 1191:129-130.

[27] McDiarmid D.L. A general criterion for high –cycle multiaxial fatigue failure. Fatigue Fracture Engineering Material Structures 1991;14:429-453.

[28] Fouvry S., Elleuch K., Simeon G. Prediction of crack nucleation under partial slip fretting conditions, Journal of Strain Analysis 2002; 37(6):549-564.

[29] Nowell D, Hills DA. Open cracks at or near free edges. J Strain Analysis 1987; 22 (3): 177-185.

[30] Bueckner HF. The propagation of cracks and the energy of elastic deformation. Trans ASME 1958; 80:1225-1230.

[31] Hills D. A., Kelly P.A., Dai D.N., Korsunsky A.M., Solution of Crack Problems: The distributed dislocation technique, Kluwer Academic Publishers, 1996.

[32] Fouvry S., Nowell D., Kubiak K., Hills D.A. Prediction of fretting crack propagation based on a short crack methodology. Engineering Fracture Mechanics 2008; 75 (6):1605-1622.

[33] S. Fouvry, V. Fridrici, C. Langlade, Ph. Kapsa, L. Vincent, Palliatives in Fretting : A dynamical approach, Tribology International 2006;39:1005–1015.

FIGURE CAPTION

Fig. 1: Illustration of the Fretting Fatigue phenomenon: (a) Schematic of the combined contact and bulk stress (NB: fatigue and contact loading are usually coupled and a function of the assembly stiffness); (b) Illustration of the different cracking damage evolutions which can be observed under fretting loading conditions.

Fig. 2: Illustration of the Fretting-Fatigue Mapping concept defined for partial slip conditions.

Fig. 3 : Illustration of the experimental strategy applied to identify the tribological properties, crack nucleation and crack arrest conditions under plain fretting and fretting-fatigue loading conditions.

Fig. 4: Illustration of the pressure and shear stress field distributions under Fretting-Fatigue condition : Loading ($\sigma_{FATIGUE} = \sigma_a \Rightarrow Q = +Q^*$), Unloading ($\sigma_{FATIGUE} = -\sigma_a \Rightarrow Q = -Q^*$).

Fig. 5 : Illustration of the determination of the maximum amplitude of the second invariant of the stress deviator ($\sqrt{J_2(t)}$) defined as ξ_a (with Φ' projection of Φ on the deviatoric plane).

Fig. 6 : Experimental identification of the threshold tangential force amplitude(Q^*_{CN}) inducing a crack under plain fretting loading (AISI 1034, 10^6 cycles, p_{0H} = 450 MPa, a_H= 320 µm).

Fig. 7 : Illustration of the cracking risk below the interface under plain fretting conditions at the threshold crack nucleation condition (p_{0H} = 450 MPa, a_H= 320 µm, μ_t=0.85, Q^*_{CN} = 100 N/mm) defined from the Crossland criterion.

Fig. 8 : Illustration of the length scale approaches applied to integrate the stress gradient effect; ◇ : point where the representative stress state is established; ● : point the stress where is computed.

Fig. 9 : Illustration of the reverse identification approach based on the Crossland fatigue criteria to identify the representative length scale variable related to the crack nucleation process volume approach ($\ell_{3D\_Crossland}$): (a) Schematic of the stress analysis; (b) Illustration of the crack nucleation process volume determination.

Fig. 10 : Illustration of the Crack Nucleation Fretting-Fatigue Map of AISI 1034 steel (p_{0H} = 450 MPa, a_H= 320 µm, μ_t=0.85, 10^6 cycles); ○ no crack nucleation; ● crack nucleation; ■ crack nucleation threshold identified for plain fretting conditions; ▬ ▬ ▪ experimental crack nucleation boundary (▪▪▪▪▪▪▪▪ estimated evolution). Theoretical predictions (Crossland): —— conventional point stress analysis; —— Crack nucleation process volume ($\ell_{3D\_Crossland}$= 45 µm), □ Crack nucleation process surface ($\ell_{2D\_Crossland}$= 55 µm); ▲ Critical distance method ($\ell_{1D\_Crossland}$= 20 µm).

Fig. 11 : Comparison between multiaxial fatigue approaches (Experimental Crack Nucleation Fretting-Fatigue Map of AISI 1034 steel (p_{0H} = 450 MPa, a_H= 320 µm, μ_t=0.85, 10^6 cycles): ○ no crack nucleation; ● crack nucleation; ■ crack nucleation threshold identified for plain fretting conditions; ▬ ▬ ▪ experimental crack nucleation boundary (▪▪▪▪▪▪▪▪ estimated evolution); Theoretical prediction of the crack nucleation boundary : —— Crossland criterion ($\ell_{3D\_Crossland}$= 45 µm); —□— Dang Van criterion ($\ell_{3D\_DangVan}$ = 60 µm); —◆— McDiarmid criterion ($\ell_{3D\_McDiarmid}$ = 95 µm).

Fig. 12 : Bueckner's principle: (A) Body without crack subjected to contact load, (B) cracked body devoid of external loads but with crack line traction and shear equal and opposite to the crack line stress in (A). (Modified crack coordinates system defined from the (X, Y) contact system: $\hat{x}$ =y/a; $\hat{y}$ =x/a-1).

Fig. 13 : Illustration of the short crack arrest methodology (AISI 1034, ΔK_0 = 7 MPa√m and b_0 = 170 µm) ; ▬: K-T's approximation of the crack arrest boundary; — El Haddad's approximation of the crack arrest boundary; ▲▲ Severe Fretting Fatigue loading inducing propagation until failure; ▫▫ Smooth Fretting Fatigue loading promoting a crack arrest (○ Crack arrest condition predicted by K-T's approximation; □ Crack arrest condition predicted by El Haddad's approximation).

Fig. 14 : Illustration of the Crack Arrest Fretting-Fatigue Map of AISI 1034 steel (p_{0H} = 450 MPa, a_H= 320 µm, μ_t=0.85, 10^7 cycles): ■: broken specimen; □: unbroken specimen; ▪▪▪▪▪: experimental boundary defining the crack arrest condition; Theoretical prediction : (a) K-T's short crack arrest approximation, (b) El Haddad's short crack arrest approximation;

– – – -: $\Delta K_{eff\_A} = \sqrt{\Delta K_I^2 + \Delta K_{II}^2}$; ———: $\Delta K_{eff\_B} = \sqrt{K_{Imax}^2 + \Delta K_{II}^2}$;

———: $\Delta K_{eff\_C} = \sqrt{K_{Imax}^2 + K_{IImax}^2}$; -◆- : $\Delta K_{eff\_D} = K_{Imax}$.

Fig. 15 : Evolution of the maximum crack length related to the crack arrest condition as a function of the applied effective SIF range value $\Delta K_{eff\_B} = \sqrt{K_{Imax}^2 + \Delta K_{II}^2}$ (AISI 1034); ◆: plain fretting test (Table 2); ◇ : Fretting Fatigue test (Table 4) ; ——: K.T.'s approximation of the short crack arrest threshold; ——:El Haddad's approximation of the short crack arrest threshold.

Fig. 16 : Material Response Fretting-Fatigue Map of AISI 1034 steel (p_{0H} = 450 MPa, a_H= 320 µm, μ_t=0.85): ○ : no crack nucleation (10^6 cycles); ●: crack nucleation (10^6 cycles); ◆: crack nucleation threshold identified for plain fretting conditions (10^6 cycles); ■ : broken specimen (10^7 cycles); □ : unbroken specimen (10^7 cycles); ——: theoretical crack nucleation boundary (Crossland, ℓ_{3D} = 45 µm) ; ——: theoretical crack arrest boundary (El Haddad's-short crack arrest methodology using a mixed-mode approximation taking into account the closure effect but neglecting crack face friction (ΔK_{eff_B})).

Fig. 17 : Theoretical Fretting-Fatique Map of 30NiCrMo8 steel (σ_d =420 MPa, ΔK_0 = 3 MPa$\sqrt{m}$); Contact loading : p_{0H} = 450 MPa, a_H= 320 µm, μ_t=0.85; Fatigue Loading normalized versus the AISI 1034 fatigue limit ($\sigma_{d(AISI1034)}$ = 270 MPa): ——: theoretical crack nucleation boundary (Crossland, ℓ_{3D} = 10 µm) ; ——: theoretical crack arrest boundary (El Haddad's-short crack arrest methodology using a mixed-mode approximation taking into account the closure effect but neglecting crack face friction (ΔK_{eff_B})).

Fig. 18 : Comparison between AISI 1034 and 30NiCrMo8 Fretting-Fatigue cracking responses (upper limits),(contact loading : p_{0H} = 450 MPa, a_H= 320 µm, μ_t=0.85; fatigue loading normalized versus the AISI 1034 fatigue limit ($\sigma_{d(AISI1034)}$ = 270 MPa)); ——: AISI 1034 steel (crack arrest boundary); ——: 30NiCrMo8 steel (crack arrest boundary); – – : 30NiCrMo8 steel (crack nucleation boundary).

Fig. 19 : Impact of surface treatments on fretting cracking after [14] (◇: 30NiCrMo8 steel; ▲: 30NiCrMo8 steel + shot peening; ●: 30NiCrMo8 steel + shot peening+ WC-Co HVOF coating); (a) Plain fretting test: plane / cylinder (52100, R=40mm) contact, P = 400 N/mm, $p_{0(Hertz)}$=600 MPa, 250000 cycles; (b) Fretting Fatigue test : plane / sphere (52100, R=100mm) contact, P=886 N, Q*= Cst= ± 886 N, $p_{0(Hertz)}$=600 MPa).

Fig. 20 : Schematic Fretting Fatigue Map's description of palliative strategies against fretting fatigue cracking : (a) Application of surface coating to extend the safe crack nucleation domain; (b) Application of an in depth surface treatment to extend the crack arrest domain; (c) Combined crack nucleation / crack arrest strategy (—— crack nucleation boundary, —— crack arrest boundary, —— ultimate safe cracking limit).

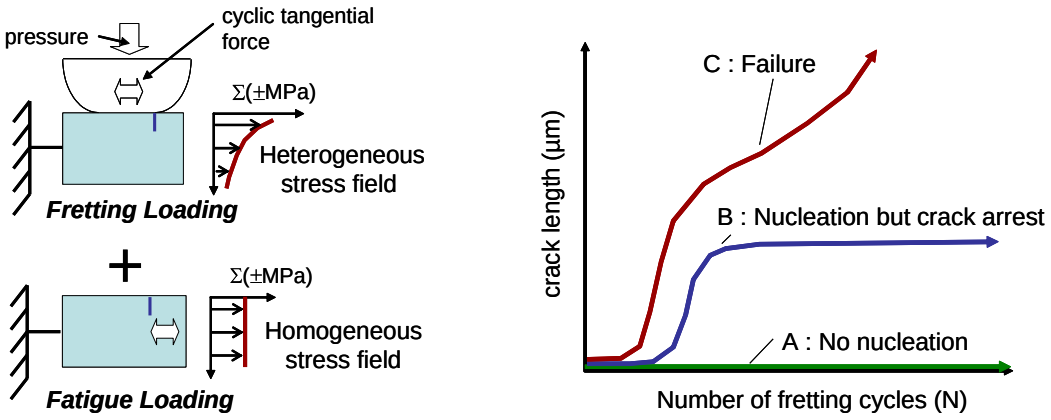
pressure
cyclic tangential force
Σ(±MPa)
Heterogeneous stress field
Fretting Loading
Σ(±MPa)
Homogeneous stress field
Fatigue Loading
C : Failure
B : Nucleation but crack arrest
A : No nucleation
crack length (µm)
Number of fretting cycles (N)

(a) (b)

Fig. 1

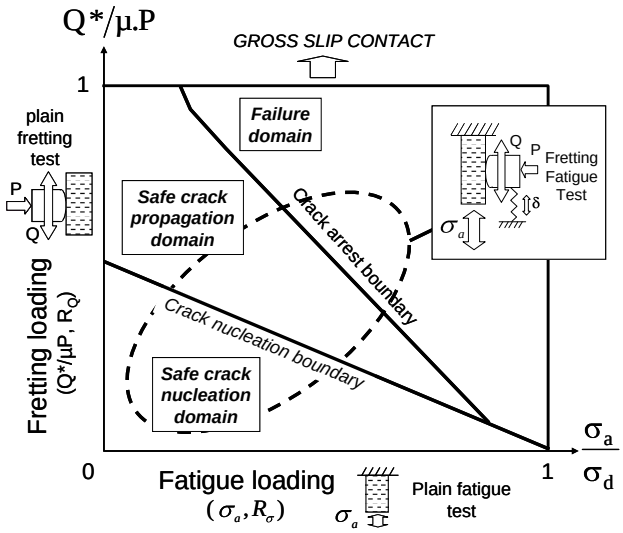
Q*/µ.P
GROSS SLIP CONTACT
1
plain fretting test
P
Q
Failure domain
Safe crack propagation domain
Crack arrest boundary
Crack nucleation boundary
Safe crack nucleation domain
Q
P
Fretting Fatigue Test
δ
σa
Fretting loading (Q*/µP, RQ)
0
Fatigue loading (σa, Rσ)
σa
Plain fatigue test
1
σa
σd

Fig. 2

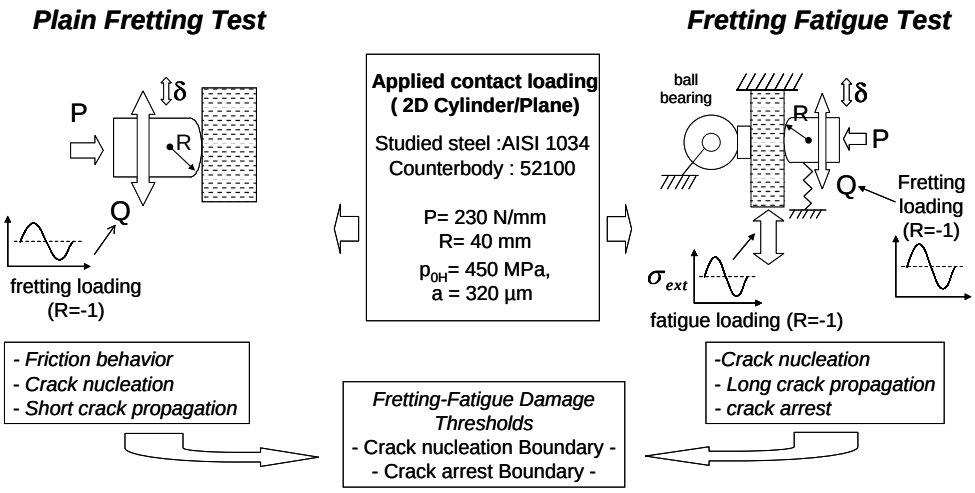
Plain Fretting Test
Fretting Fatigue Test
Applied contact loading
(2D Cylinder/Plane)
Studied steel :AISI 1034
Counterbody : 52100
P= 230 N/mm
R= 40 mm
p0H= 450 MPa,
a = 320 µm
P
R
δ
Q
fretting loading
(R=-1)
ball
bearing
Fretting
loading
(R=-1)
σext
fatigue loading (R=-1)
- Friction behavior
- Crack nucleation
- Short crack propagation
Fretting-Fatigue Damage
Thresholds
- Crack nucleation Boundary -
- Crack arrest Boundary -
-Crack nucleation
- Long crack propagation
- crack arrest

Fig. 3

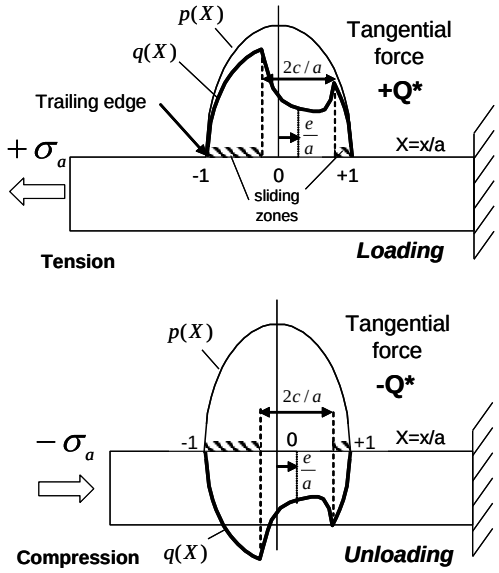
p(X)
q(X)
Tangential
force
+Q*
2c / a
Trailing edge
e/a
+σa
X=x/a
-1
0
+1
sliding
zones
Tension
Loading
p(X)
Tangential
force
-Q*
2c / a
-σa
-1
0
+1
X=x/a
e/a
Compression
q(X)
Unloading

Fig. 4

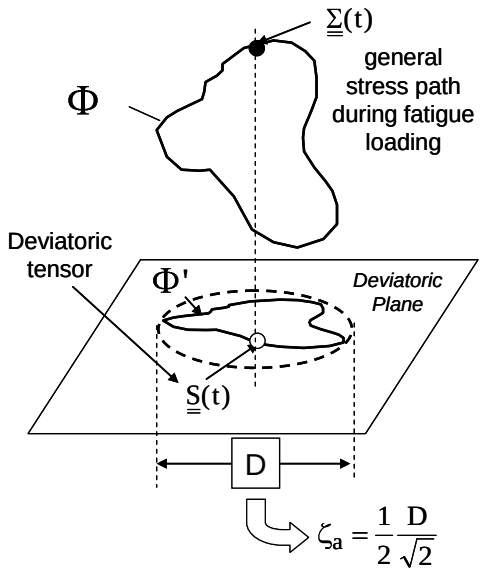
Σ(t)
general
stress path
during fatigue
loading
Φ
Deviatoric
tensor
Φ'
Deviatoric
Plane
S(t)
D
$\zeta_a = \frac{1}{2}\frac{D}{\sqrt{2}}$

Fig. 5

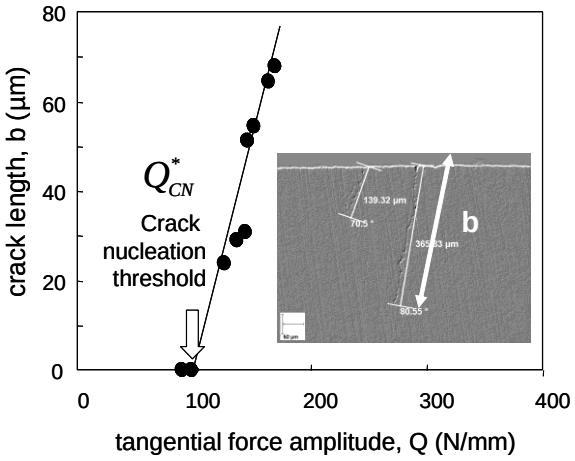
crack length, b (μm)
tangential force amplitude, Q (N/mm)
0
20
40
60
80
0
100
200
300
400
Q^*_{CN}
Crack
nucleation
threshold
b

Fig. 6

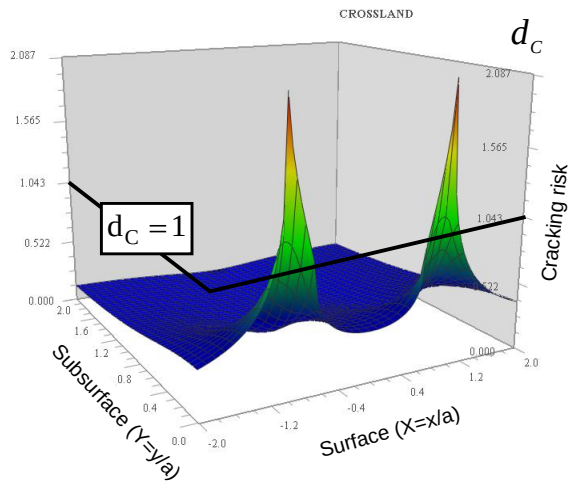
CROSSLAND
d_C
2.087
1.565
1.043
0.522
0.000
$d_C = 1$
Cracking risk
Subsurface (Y=y/a)
Surface (X=x/a)

Fig. 7

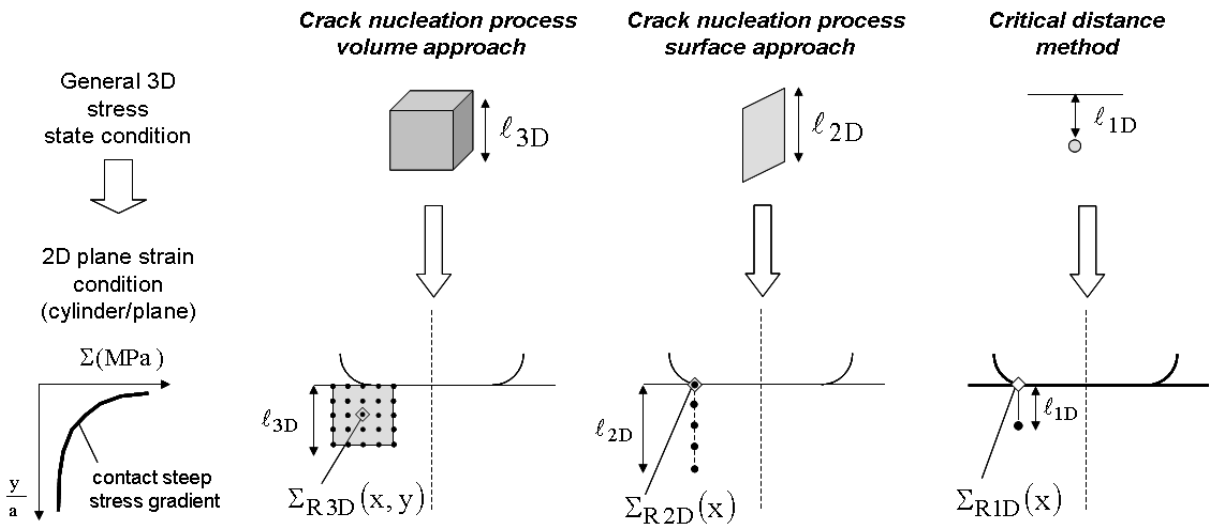
General 3D stress state condition
2D plane strain condition (cylinder/plane)
Σ(MPa)
y/a
contact steep stress gradient
Crack nucleation process volume approach
Crack nucleation process surface approach
Critical distance method
ℓ_{3D}
ℓ_{2D}
ℓ_{1D}
$\Sigma_{R\,3D}(x, y)$
$\Sigma_{R\,2D}(x)$
$\Sigma_{R1D}(x)$

Fig. 8

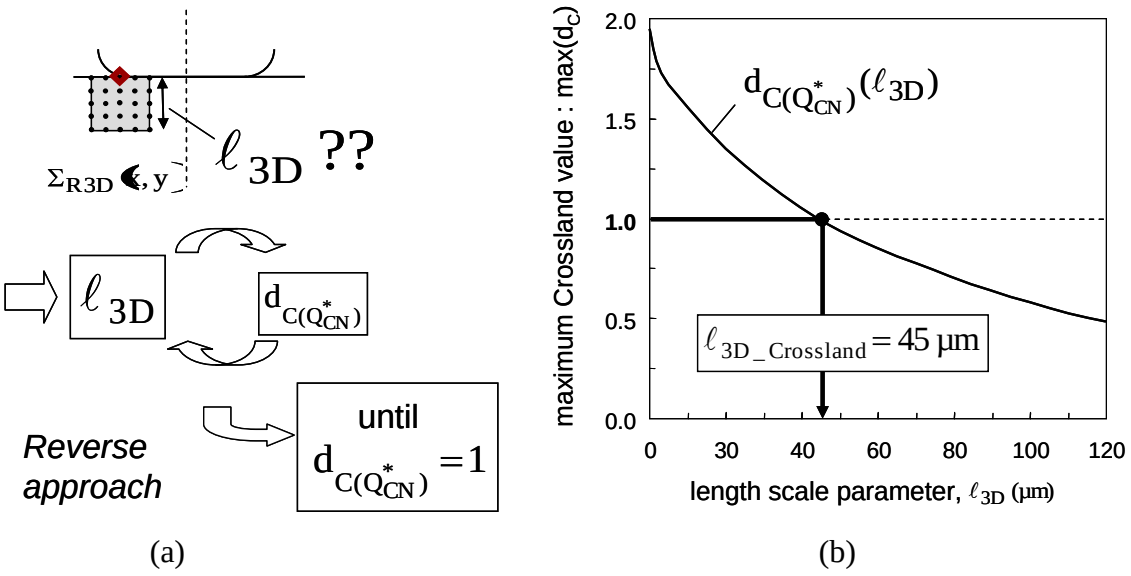
ℓ_{3D} ??
Σ_{R3D} (ξ, y)
ℓ_{3D}
$d_{C(Q^*_{CN})}$
Reverse approach
until $d_{C(Q^*_{CN})} = 1$
(a)
maximum Crossland value : max(d_C)
$d_{C(Q^*_{CN})}(\ell_{3D})$
$\ell_{3D\_Crossland} = 45\ \mu m$
length scale parameter, ℓ_{3D} (μm)
(b)

Fig. 9

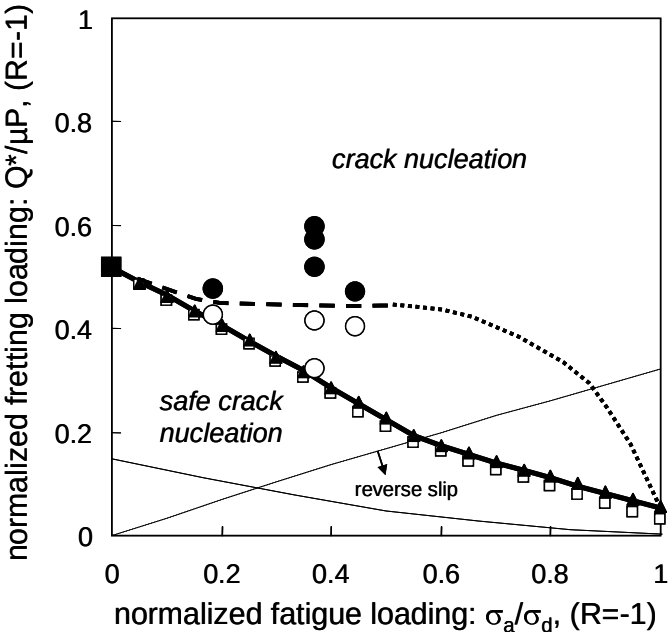
normalized fretting loading: Q*/μP, (R=-1)
crack nucleation
safe crack nucleation
reverse slip
normalized fatigue loading: σ_a/σ_d, (R=-1)

Fig. 10

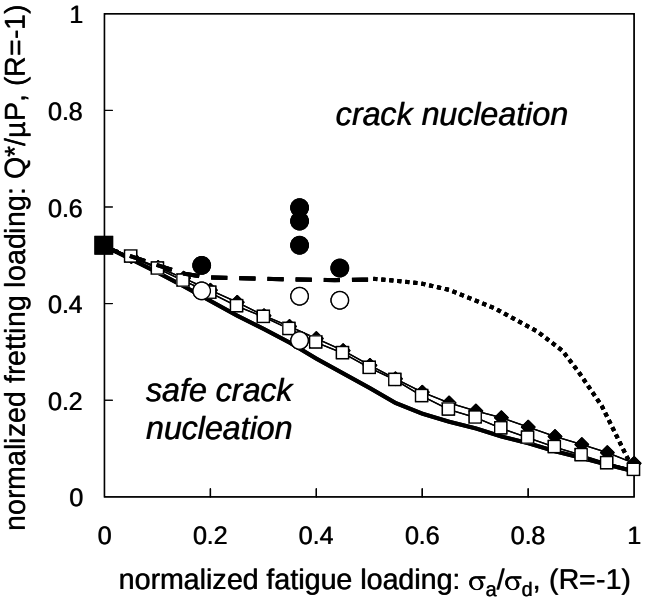
normalized fretting loading: Q*/μP, (R=-1)
normalized fatigue loading: σa/σd, (R=-1)
crack nucleation
safe crack nucleation
0
0.2
0.4
0.6
0.8
1

Fig. 11

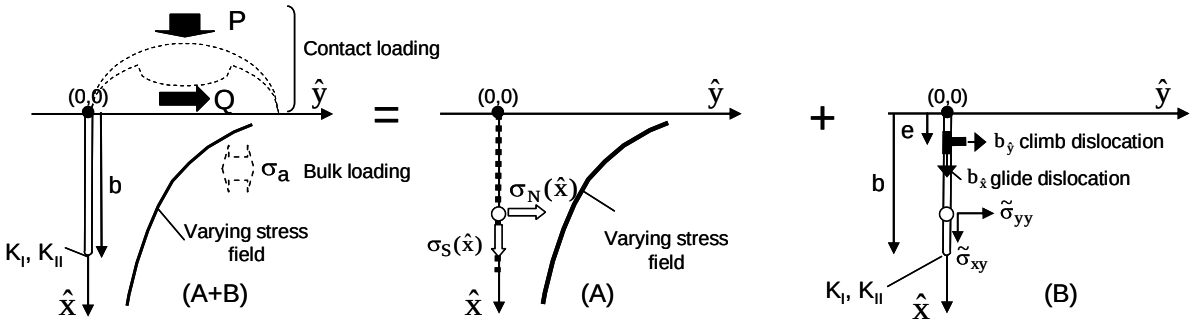
P
Contact loading
(0,0)
Q
ŷ
x̂
b
σa
Bulk loading
Varying stress field
K_I, K_II
(A+B)
=
σN(x̂)
σS(x̂)
(A)
+
e
b_ŷ climb dislocation
b_x̂ glide dislocation
σ̃yy
σ̃xy
(B)

Fig. 12

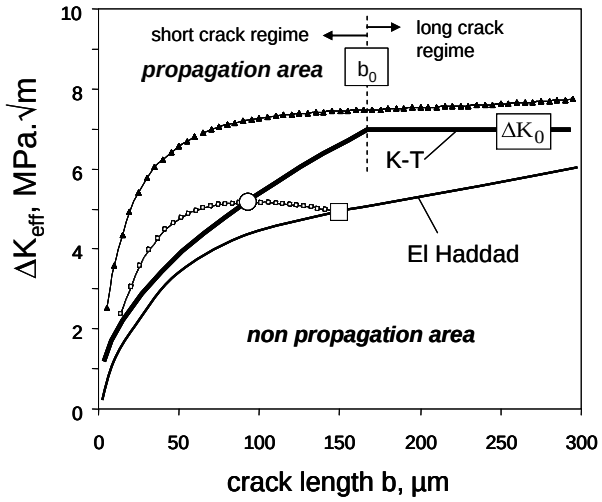

Fig. 13

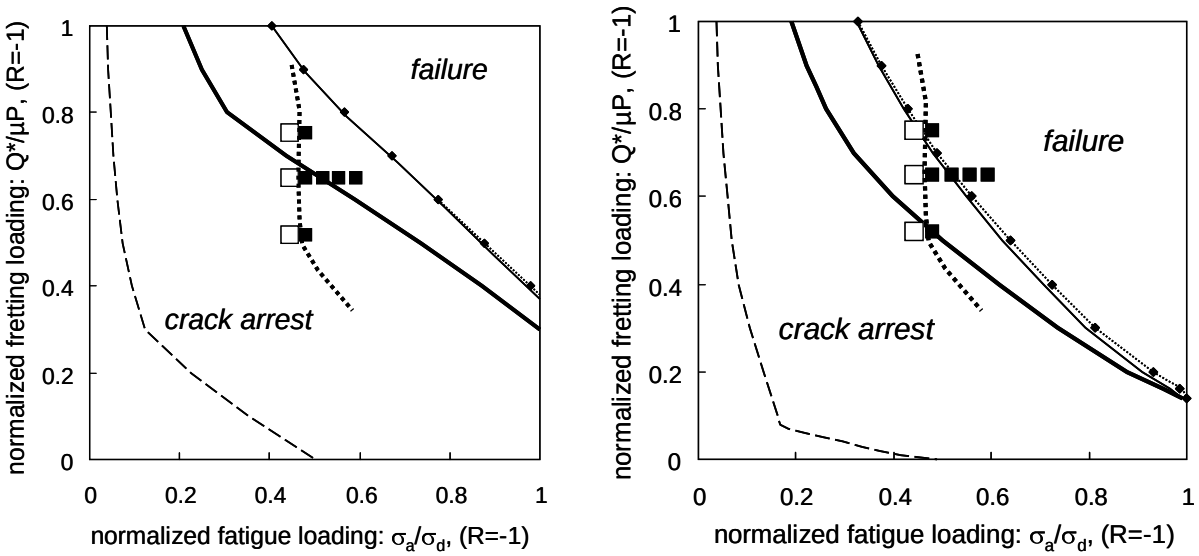

(a) (b)

Fig. 14

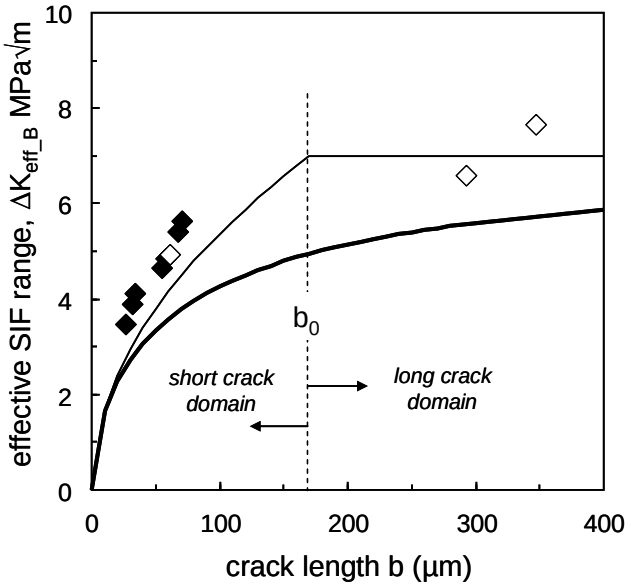
effective SIF range, ΔK_{eff_B} MPa$\sqrt{m}$
crack length b (μm)
b_0
short crack domain
long crack domain
0
2
4
6
8
10
0
100
200
300
400

Fig. 15

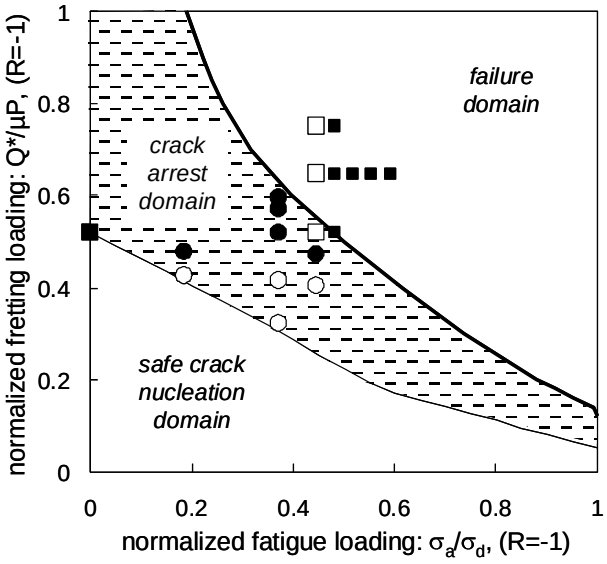
normalized fretting loading: Q*/μP, (R=-1)
normalized fatigue loading: σ_a/σ_d, (R=-1)
failure domain
crack arrest domain
safe crack nucleation domain
0
0.2
0.4
0.6
0.8
1

Fig. 16

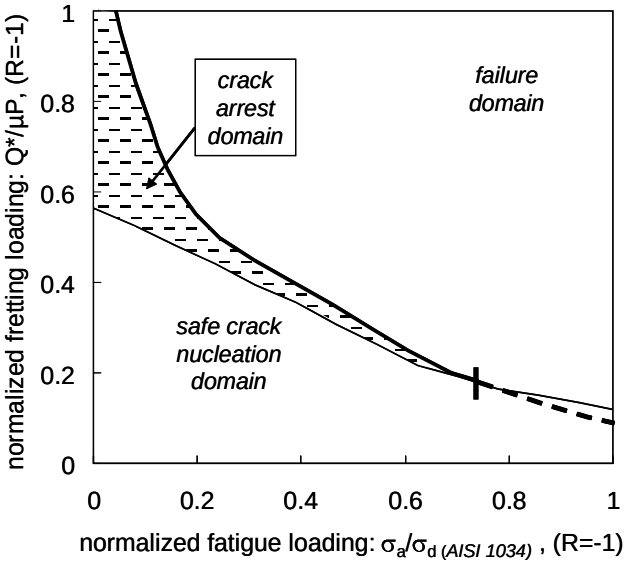
crack
arrest
domain
failure
domain
safe crack
nucleation
domain
normalized fretting loading: Q*/μP, (R=-1)
normalized fatigue loading: σa/σd (AISI 1034) , (R=-1)
0
0.2
0.4
0.6
0.8
1

Fig. 17

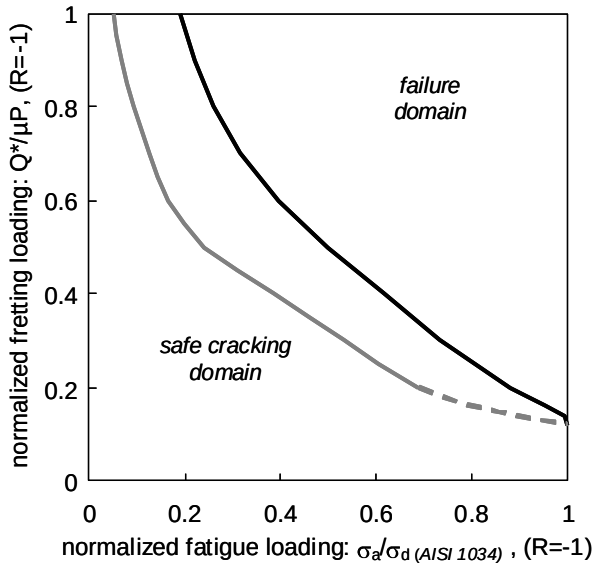
failure
domain
safe cracking
domain
normalized fretting loading: Q*/μP, (R=-1)
normalized fatigue loading: σa/σd (AISI 1034) , (R=-1)
0
0.2
0.4
0.6
0.8
1

Fig. 18

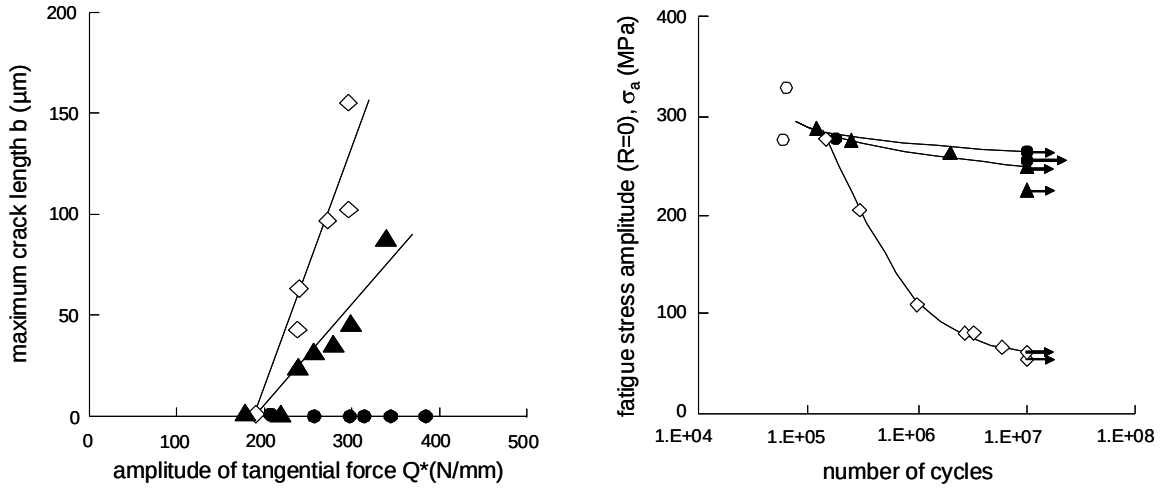

(a) (b)

Fig. 19

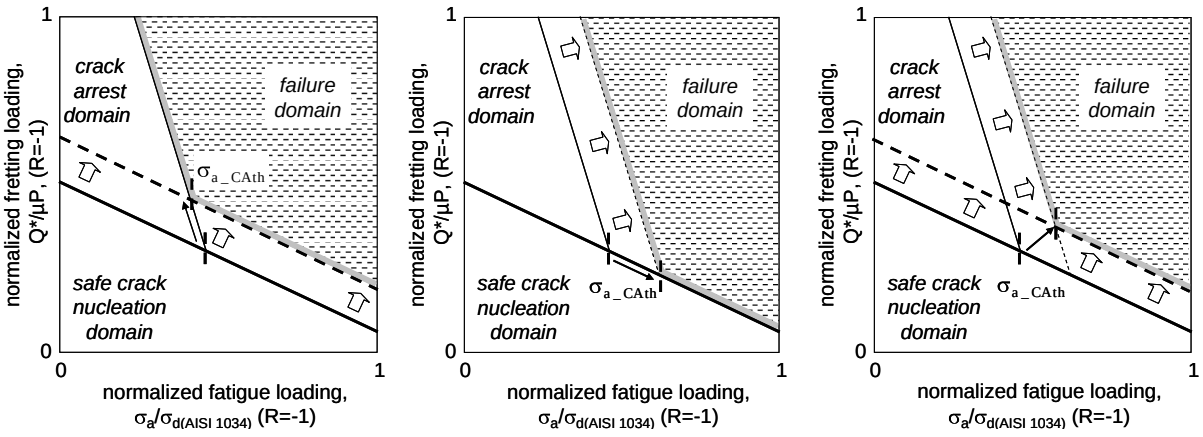

(a) (b) (c)

Fig. 20

TABLES

Table 1 : Mechanical properties of the materials

Materials	AISI 1034 [13] (plane)	30NiCrMo8 [14] (plane)	52100 (cylinder)
Young's modulus E (GPa)	200	200	210
Poisson's coefficient ν	0.3	0.3	0.3
Yield stress σ_Y (0.2%) (MPa)	350	740	1700
Ultimate stress σ_{UTS} (MPa)	600	890	2000
Bending Fatigue limit σ_d (MPa) (R=-1, 10^7 cycles)	270 ± 10	420 ± 10	-
Shear fatigue limit τ_d (MPa) (R=-1, 10^7 cycles)	170 ± 10	265 ± 10	-
long crack threshold ΔK_0 (R=-1) (MPa$\sqrt{m}$)	7 ± 1	4 ± 1	-
Long crack length transition b_0 (µm) estimated from [11, 12]	170	23	-

Table 2 : Evolution of the experimental crack length under plain fretting conditions as a function of the tangential force amplitude (AISI 1034 , 10^6 cycles, p_{0H} = 450 MPa, a_H= 320 µm).

Tangential force amplitude Q* [N/mm] (R=-1)	90	98	126	137	144	146.0	151	164	169
Longest crack length observed b(µm)	0	0	24	29	31	52	55	65	68

Table 3: Studied Fretting Fatigue test conditions (AISI 1034).

Fretting Fatigue Test (10^6 cycles)	Fatigue stress amplitude : σ_a [MPa] (R=-1)	Tangential force amplitude Q* [N/mm] (R=-1)	Cross section Examination
FF1	50	92	CRACK
FF2	50	82	NO CRACK
FF3	100	115	CRACK
FF4	100	110	CRACK
FF5	100	100	CRACK
FF6	100	80	NO CRACK
FF7	100	62	NO CRACK
FF8	120	91	CRACK
FF9	120	78	NO CRACK

Table 4 : Studied Fretting Fatigue test conditions (AISI 1034).

Fretting Fatigue Test (10^7 cycles)	Fatigue stress amplitude : σ_a [MPa] (R=-1)	Tangential force amplitude Q* [N/mm] (R=-1)	Maximum crack length expertised : b (µm)
FF10	120	145	344
FF11	120	125	290
FF12	120	100	59
FF13	130	145	broken
FF14	130	125	broken
FF15	130	100	broken
FF16	140	125	broken
FF17	150	125	broken
FF18	160	125	broken